

Access provided by:  
**INSTITUTE OF COMPUTING  
 TECHNOLOGY CAS**  
 Sign Out

[Browse](#)[My Settings](#)[Get Help](#)[Abstract](#)[Authors](#)[Figures](#)[Multimedia](#)[References](#)[Cited By](#)[Keywords](#)

## Short-Range Doppler-Radar Signatures from Industrial Wind Turbines: Theory, Simulations, and Measurements

Industrial wind turbines are large constructions that require in-field monitoring. In this paper, short-range Doppler radar signatures of wind turbines are both mathematically analyzed and practically verified through simulations and experiments. Two custom-designed radar prototypes that operate at the C and K bands, respectively, are employed in the acquisition campaign. The unique features of the radar signal-in-particular, some observed energetic flashes in the time-Doppler map-appear as curved lines for specific acquisition scenarios and/or for nonstraight blades. Furthermore, it is demonstrated that the use of high-frequency radar systems is beneficial in terms of improved spectrogram resolution. Experimental results coming from a 50-m-height wind turbine and a curved-blade 12-m-height turbine are also discussed, in this paper, in the context of the provided theoretical and simulation frameworks. This paper paves the way for noncontact structural health monitoring of industrial-type wind turbines through portable low-cost Doppler radar sensors.

This paper appears in: IEEE Transactions on Instrumentation and Measurement, Issue Date: Sept. 2016, Written by: Jos?-Mar?a Mu?oz-Ferreras; Zhengyu Peng; Yao Tang; Roberto G?mez-Garc?a; Daan Liang; Changzhi Li

© 2016 IEEE

### SECTION I

#### INTRODUCTION

With the ever-increasing production of ecologically sustainable energy from wind, wind farms and their constituent turbines are becoming larger and larger [1] [2] [3] [4]. Wind turbines can be huge structures that are exposed to enormous mechanical tensions and strains [5]. In addition to standard structural health monitoring (SHM) actions for them [6] [7] [8] [9] [10], portable low-cost Doppler radars may be used as noncontact short-range wireless sensor devices to complement these tasks [11], [12]. To that long-term purpose, the theoretical analysis of these short-range signatures, along with its validation with simulated and experimental results, become of paramount importance.

Doppler radars have been employed to monitor the health of civil facilities—such as skyscrapers, bridges, pipes, or big stadiums. For example, they can precisely determine possibly arising vibrations and long-term motions in these structures [13] [14] [15]. Indeed, this monitoring serves as a diagnosis of facility's current health conditions to increase the human safety and to obtain valuable information for future constructions in potentially harsh environments, such as in earthquake-sensitive areas [16] [17] [18] [19] [20] [21]. In the particular case of wind turbines, an early indication of arising problems—e.g., damages in the yaw-bearing system, rupture of the blade tips, or mass imbalances due to ice accumulation—may lead to maintenance operations or even emergency shutdown actions to prevent further serious consequences to the entire system [6] [7] [8] [9] [10].

Conventional methods for the SHM of wind turbines analyze the imbalances of the rotor and undesired transversal oscillations of the nacelle [22]. In laboratory fatigue tests, the so-called acoustic emission approach establishes relations between sound waves and possible failures [23] [24] [25], whereas precise optical-based methods are exploited to determine the construction quality of the blades through the analysis of their shapes [26] [27] [28]. The employment of optical fibers embedded in the wind-turbine blades enables an in-field monitoring in terms of temperature, strain, or bending conditions [29] [30] [31].

Radar signatures for wind turbines in time-Doppler maps have been studied and experimentally validated in previous works [32] [33] [34] [35] [36] [37] [38] [39] [40] [41] [42] [43] [44]. Long-distance analysis and measures have revealed the appearance of the so-called micro-Doppler effects, such as energetic time-narrow flashes occurring when one blade is orthogonal to the propagation direction of the transmitted signal [37] [38] [39] [40] [41] [42] [43] [44]. Also, some experiments for near laboratory models and low-frequency systems have been conducted to confirm that nonstraight blades lead to curved flashes [32] [33] [34] [35] [36]. Interestingly, many of the previous works have additionally shown smaller returns corresponding to the blade tips, which are usually referred to as halos.

A novelty of this paper rests in the theoretical study of Doppler radar signatures from in-field industrial wind turbines in short-range acquisition scenarios. Mathematical analysis together with simulations makes emphasis on the echo differences when the illumination aspect angle changes, and when the blades do not follow a conventional straight shape. In particular, a parabolic model for curved blades is proposed, simulated, and analyzed. The obtained curved flashes for this type of blades are explained in terms of the coherent sum of the signal contributions associated with the blade scatterers. The suggested

novel signal-based modeling enables to interpret the spectrogram features beyond conventional explanations usually based on perpendicular incidence and diffraction phenomena.

The presented theoretical results are validated through innovative in-field experiments for a 50-m-height and a 12-m-height wind turbine in the American Wind Power Center, Lubbock, TX, USA. The latter has curved blades, which is suitable to verify the aforementioned parabolic model. In particular, some curved returns—referred to here as hook flashes—are observable here for the first time and can be used to obtain a curvature measure for the blades—in close connection with the parabolic model. The reported measurements were carried out through two novel custom-designed Doppler radar systems: a  $C$ -band prototype working at 5.8 GHz and a  $K$ -band Doppler radar with an operation frequency of 24 GHz. For completeness, both radar systems are briefly described. Besides, some additional features observed in the spectrograms for the 24-GHz sensor—i.e., flash mirroring due to in-phase/quadrature ( $I/Q$ ) mismatches and unconventional quasi-sinusoidal signatures, which may be attributed to scattering discontinuities—have been verified through simulation.

As an important contribution, the provided study enables to conclude that it is beneficial to deploy the radar system, so that the Doppler frequency becomes the maximum possible with the purpose of circumventing spurious flash curvature for straight blades. Also, the use of high-frequency systems is preferred in order to have finely detailed high-resolution spectrograms. Finally, considering that curved blades lead to curvature in their associated flashes, unconventional bending of straight blades might be detected for SHM purposes. In relation to the latter, further research must focus on analyzing the impact of the actual blade shapes and their bending limits in the flash appearance.

It should also be noted that this paper is a considerably expanded version of the results reported in [11] and [12]. Nikoubin *et al.* [11] presented some preliminary experimental results for the 50-m-height wind turbine when illuminated by a commercial single-channel radar gun. Muñoz-Ferreras *et al.* [12] showed some simulations for straight blades. The signal-based mathematical framework, the parabolic model, the new simulations, the measurements for the 12-m-height curved-blade wind turbine, and the employment of two novel radar prototypes are new accomplishments in this paper.

The rest of this paper is structured as follows. Section II provides the theoretical formulation and the signal modeling for a Doppler radar illuminating a short-distance wind turbine. The justification for the appearance of the flashes and the halos for both straight and curved blades is also given in Section II. Simulation results that confirm the expounded theoretical framework are provided in Section III. A brief description of the Doppler radar systems utilized in the experiments can be found in Section IV. Section IV also describes the field test setup and the obtained measurement results, which are in close agreement with the simulations. Finally, the most relevant conclusions of this paper are set out in Section V.

## SECTION II THEORETICAL APPROACH

In this section, the mathematical modeling of the received signal for Doppler radars when illuminating a wind turbine is presented. The appearance of the flashes and the halos associated with the blade tips is also justified. Furthermore, a parabolic model for the shape of curved blades is provided and discussed.

### A. Signal Modeling

Consider a moving point-scatterer target whose range from the Doppler radar is the time-varying function  $R(t)$ , where  $t$  is the time. The complex-valued analytic received signal  $s_{Rx}(t)$  can be written as

$$s_{Rx}(t) = \sigma \exp \left( j2\pi f_c \left( t - \frac{2R(t)}{c} \right) \right) \quad (1)$$

[TeX Source](#)

where  $\sigma$  is its amplitude,  $f_c$  is the frequency of the transmitted sinusoidal signal, and  $c$  is the speed of light.

Conventional Doppler radars obtain the  $I/Q$  components of the received signal [45]. To that purpose, the returned echoes are mixed with the  $I/Q$  replicas of the transmitted tone. After the signal acquisition with a two-channel analog-to-digital converter, the components  $I$  and  $Q$  are combined to form a complex-valued signal—usually referred to as the complex-valued baseband signal. This baseband signal  $s_b(t)$  for the considered point scatterer can be expressed as [45]

$$s_b(t) = \sigma \exp \left( -j \frac{4\pi}{\lambda} R(t) \right) \quad (2)$$

[TeX Source](#)

where  $\lambda$  is the wavelength for the transmitted continuous-wave (CW) tone—i.e.,  $\lambda = c/f_c$ .

If many scatterers are considered, the baseband signal can be simply written as the following sum of the different contributions:

$$s_b(t) = \sum_{k=1}^K \sigma_k \exp \left( -j \frac{4\pi}{\lambda} R_k(t) \right) \quad (3)$$

[TeX Source](#)

where  $K$  is the number of scatterers, and  $\sigma_k$  and  $R_k(t)$  are the amplitude and the time-varying range for the  $k$ th scatterer, respectively.

### B. Flashes and Halos for Rotating Blades

Human-made targets, such as the blades of a wind turbine, are usually shaped by smooth surfaces. Fig. 1 schematically shows a blade of arbitrary shape at a certain angular position illuminated by a near Doppler radar. A segment of the blade of length  $L_{\text{LOS}}$ —note that this length is defined along the line-of-sight (LOS) of the radar—is also shown in Fig. 1.

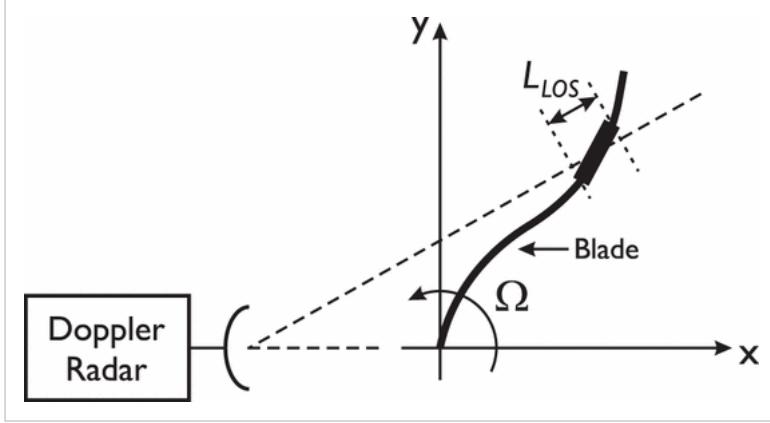


**Fig. 1.** Arbitrary-shape blade illuminated by a near Doppler radar. A segment of along-the-LOS length  $L_{\text{LOS}}$  is emphasized.

If the segment is not perpendicular to the propagation direction of the transmitted signal at a specific time  $t$ , its along-the-LOS length is much greater than the wavelength ( $L_{\text{LOS}} \gg \lambda$ ). This hypothesis can be made, because big wind turbines and high-frequency radar systems (i.e., with a small wavelength) are assumed here. Furthermore, if the segment under study is not situated in the blade tip, the signal contributions in (3) from the segment scatterers can be seen as vectors in the complex plane with uniform phases between 0 and  $2\pi$  rad, since the range to the scatterers changes at least in one wavelength [44]. Since it is reasonable to attribute the same amplitude to these scatterers of the smooth segment—i.e.,  $\sigma_k = \sigma$ , the sum in (3) is equal to zero for this situation—destructive interference—and no returns are observable. Conversely, if the segment—still located in the middle of the blade—is perpendicular to the propagation direction of the transmitted signal, its length  $L_{\text{LOS}}$  is necessarily smaller than a wavelength. Thus, by noting that the radar range to the scatterers is now a constant, the vector sum in (3) leads now to a large echo—constructive interference—if the curvature of the blade is not extreme. These large returns are observed as flashes in the received signal. Note that a simpler alternative explanation for the existence of these flashes comes from the fact that the surface only backscatters a significant signal for perpendicular incidence [32] [33] [34] [35] [36]. However, the former justification is preferred in this paper, since (3) is the basis for the simulations performed in Section III, which are in fair agreement with the experiments.

Regarding the blade tip, the length  $L_{\text{LOS}}$  of a segment located at the tip cannot be larger than the employed wavelength  $\lambda$ . As a result, the sum in (3) does not group together all the vectors with phases between 0 and  $2\pi$  rad. This means that a noncomplete destructive interference can be attained for the tip and, hence, a weak return—i.e., the tip halo—is identifiable during all the illumination time. If the interference were completely destructive, the halos would not exist, but these returns have been observed many times in the past [32] [33] [34] [35] [36] [37] [38] [39] [40] [41], [43], [44]. Note that this signal-based justification also permits to explain that a higher frequency gives rise to a weaker return for the tip, since the scatterers contributing to the tip return in (3) are less—i.e.,  $L_{\text{LOS}}$  is smaller. Simpler explanations available in the technical literature have interpreted the tip halo as a diffraction phenomenon [32] [33] [34] [35] [36].

The tip halo describes a sinusoidal curve in the time-Doppler map in long-distance scenarios. As a proof of that, note that the range from a far radar sensor to the blade tip—it is assumed here that the rotation plane contains the LOS—can be approximated as

$$R_t(t) \approx R_{rc} + R_{ct} \sin(\Omega t + \phi_t) \quad (4)$$

[TeX Source](#)

where  $R_{rc}$  is the distance from the radar to the rotation center,  $\Omega$  is the angular speed,  $R_{ct}$  is the rotation radius for the tip, and  $\phi_t$  is the initial angle of the tip in the rotation plane.

The Doppler history for the blade tip  $f_{\text{Dop},t}(t)$  can be obtained after applying the first derivative to the phase in (2) with respect to time  $t$  as follows:

$$f_{\text{Dop},t}(t) = -\frac{2}{\lambda} \cdot \frac{dR_t(t)}{dt} = -\frac{2R_{ct}\Omega}{\lambda} \cos(\Omega t + \phi_t) \quad (5)$$

[TeX Source](#)

which shows that the tip halo is sinusoidal for long-range scenarios. In contrast, in short-distance acquisition environments, the halos for the tips are no longer sinusoidal, but quasi-sinusoidal, since (4) and (5) are good approximations only for long-range illuminations. Note that the other blade tip (i.e., the blade root) in Fig. 1 is stationary and contributes to the zero-Doppler clutter returns.

### C. Parabolic Modeling of Blade Curvature

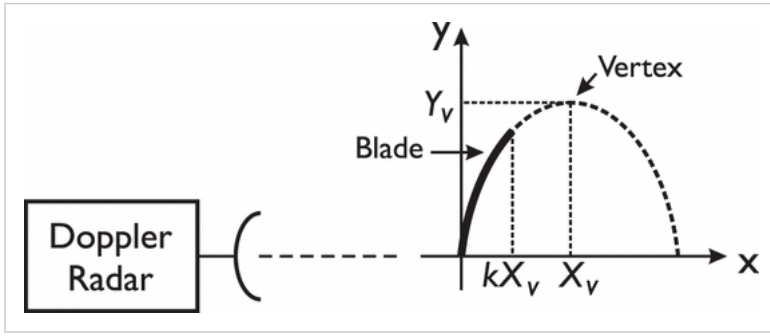
Section II-B has mathematically shown that an energetic return is obtained for every time that a segment of the blade is perpendicular to the propagation direction of the transmitted signal. In addition, it justified that a sinusoidal or quasi-sinusoidal halo for each blade tip of the wind turbine is observed in the time-Doppler map.

Fig. 2 represents a parabolic model for the shape of the blade in the local  $x$ - $y$ -coordinates. The origin of the  $x$ - $y$ -coordinate system is the rotation center. The parabola vertex has  $X_v$ - and  $Y_v$ -coordinates, whereas  $k$ —applied to  $X_v$ —measures the level of curvature considered for the blade—which is highlighted with a continuous line in Fig. 2. In this paper,  $k$  takes values between 0 and 1. The  $y$ -coordinate of a blade scatterer ( $y_s$ ) can be easily shown to be

$$y_s = -\frac{Y_v}{X_v^2}(x_s - X_v)^2 + Y_v \quad (6)$$

[TeX Source](#)

where  $x_s$  is the  $x$ -coordinate of the considered blade scatterer.



**Fig. 2.** Parabolic model for consideration of blade curvature.

For this parabolic model, the halo associated with the blade tip follows a sinusoidal or quasi-sinusoidal history regardless of the blade curvature—if the rotation rate  $\Omega$  is uniform. As an example, if  $k = 1$ , the blade tip is the vertex of the parabola. In this situation, it turns out that the blade tip is perpendicular to the propagation direction of the transmitted signal when its radial velocity is zero—i.e., when its Doppler frequency is zero. Thus, for  $k = 1$ , an energetic return is obtained when the Doppler frequency is zero, being this echo overlapped with the tip halo. When  $k < 1$ , the flash for the tip occurs for a nonzero Doppler frequency that gives rise to a characteristic hook shape for the blade flash. These results are validated through simulations and experiments in Sections III and IV, respectively.

### SECTION III SIMULATION RESULTS

In this section, several simulations are accomplished and analyzed. In particular, the acquisition scenario and the simulated results for different illumination geometries and blade curvatures are presented. Also, additional phenomena, such as  $I/Q$  mismatches and unconventional signatures, are simulated and addressed. The reported results are discussed in context with the mathematical formulation of Section II. Note that the referred simulations are based on the point-scatterer model of (3). As will be verified in Section IV, this simple modeling enables a fair agreement between simulations and measurements. More complex simulations would require sophisticated 3-D computer-aided design models for the many-wavelength-long wind turbines and electromagnetic scattering software, implying a very high computational burden [34], [37], [38].

#### A. Simulated Acquisition Scenario

The acquisition scenario for the simulations is schematically shown in Fig. 3. A Doppler radar—at the height  $H_r$  above ground—illuminates a near three-blade wind turbine. The mast length (tower height) is given by  $L_m$ , whereas  $R_c$  refers to the radius of the rotation circumference, which corresponds to the length of assumed-straight blades. The distance  $R_g$  is the ground range from the radar to the wind turbine. The blades rotate at the angular speed  $\Omega$ . Finally, the aspect angle  $\theta$  orientates the wind turbine with respect to the Doppler radar.

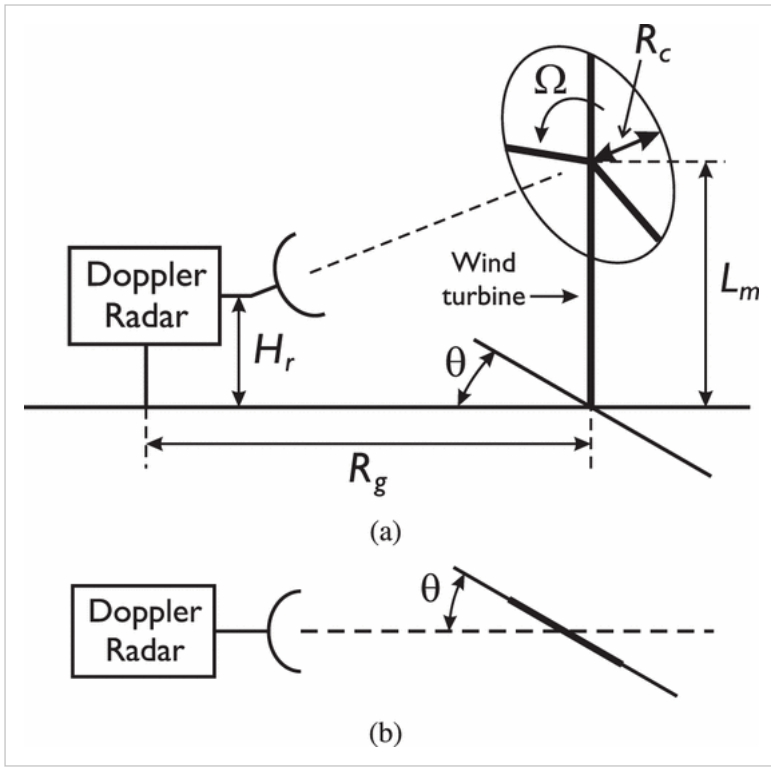


**Fig. 3.** Simulated acquisition scenario for a Doppler radar illuminating a wind turbine. (a) 3-D representation. (b) Top view.

In the simulations, it is assumed that the radar antennas are omnidirectional. On the other hand, the basis for the simulation consists in the sampling of the signal  $s_b(t)$  in (3). Moreover, after the discussions in Section II-B,  $\sigma_k = 1$  is considered, except for Section III-E. The blades and the masts are assumed to be shaped by many scatterers distributed along—straight or curved—lines, which is convenient to simulate smooth surfaces. In particular, the number of scatterers for each blade is chosen, so that the spacing among them is set to be  $\lambda/5$  in order to guarantee that the simulations are realistic [35]. Since the wind turbine is big and the employed radar wavelength is small, the number of simulated scatterers has to be large. This leads to an increase in computation time.

Table I details all the short-range scenario parameters, which are common to all the simulations presented in the next Sections III-B, III-C, III-D, and III-E. Note that the number of scatterers for the stationary mast is fixed and do not meet the  $\lambda/5$ -separation rule [35], because it only leads to zero-Doppler clutter echoes.

Radar height ( $H_r$ )	0 m
Ground range from radar to turbine ( $R_g$ )	80 m
Radius of rotation circumference ( $R_c$ )	50 m
Tower height ( $L_m$ )	80 m
Rotation rate ( $\Omega$ )	10 rpm
Number of scatterers for the mast	500
Acquisition time (CPI)	6 s
Sampling frequency ( $f_s$ )	20 kHz

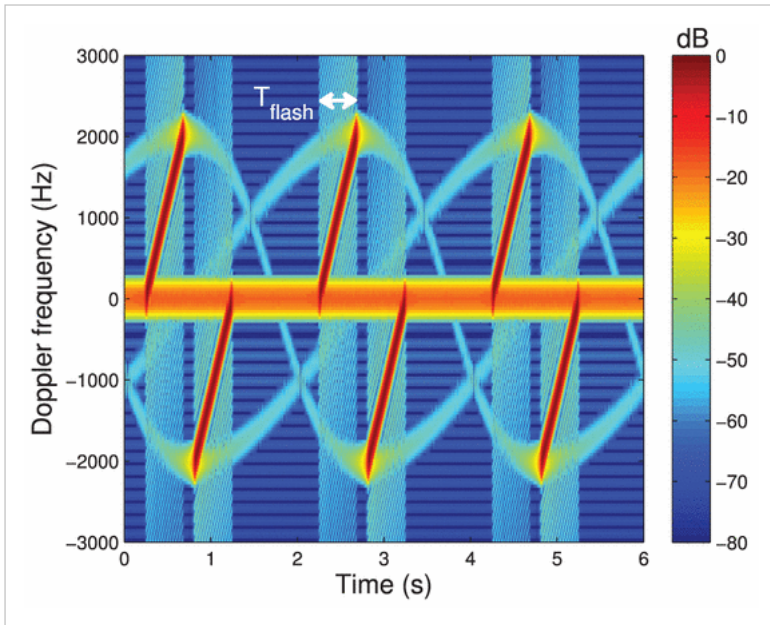
**Table I** Common Acquisition-Scenario Parameters for the Simulations

The acquisition time—i.e., the coherent processing interval—is chosen to be identical to the rotational period of the blades. Finally, the radial speed for the blade tips can be calculated as  $v_{\max} = \Omega \cdot R_c = 52.4$  m/s. For simplicity, no white Gaussian noise has been added to the simulations. Also, the parameters for the spectrogram calculation are chosen to be the same for all the cases, so that the provided comparisons are fair.

## B. Straight Blades at Different Aspect Angles

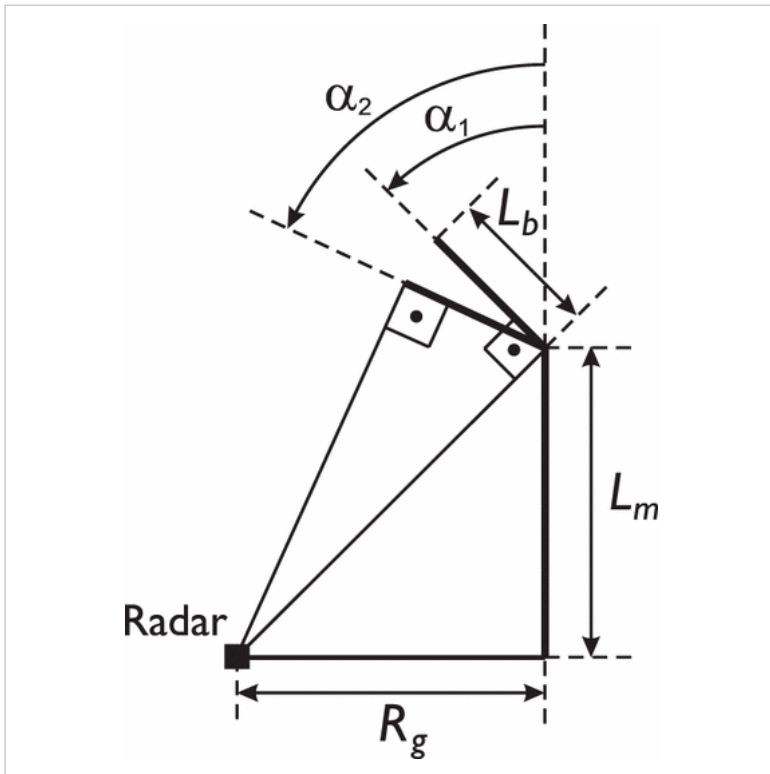
Straight blades are considered in this section. In addition, the transmitted CW tone is assumed to have a frequency of 5.8 GHz, which means that the wavelength is  $\lambda = 51.7$  mm. After applying the  $\lambda/5$ -spacing rule, the number of scatterers per blade is found to be 4833. Note that the maximum Doppler frequency is  $f_{\text{Dop,max}} = 2v_{\max}/\lambda = 2024$  Hz, which is properly acquired by the sampling frequency in Table I.

Fig. 4 details the spectrogram—i.e., the time-Doppler map—for the signal  $s_b(t)$  in (3) when the aspect angle is zero ( $\theta = 0^\circ$ ). The three flashes with positive-Doppler frequencies correspond to the approaching blades, whereas the negative-Doppler ones are associated with the receding blades. The quasi-sinusoidal halos discussed in Section II-B for this short-distance acquisition are also identifiable. Note that the zero-Doppler return corresponds to the mast.



**Fig. 4.** Spectrogram for the wind-turbine simulation for straight blades and aspect angle  $\theta = 0^\circ$ . Spectrogram parameters: Hamming window of 128 samples and fast Fourier transform (FFT) of 512 points.

The value of the maximum Doppler for the blade flashes ( $f_{\text{Dop,max}} = 2024 \text{ Hz}$ ) is visualized in Fig. 4. Also, the flashes are straight tilted lines in the spectrogram. The origin of this tilting is a short-range effect, which is not observed for long-distance acquisitions [44]. The explanation is encountered in Section II-B: each blade segment becomes perpendicular to the propagation direction of the transmitted signal at different times. Indeed, the time that the blade takes to go from angle  $\alpha_1$  to angle  $\alpha_2$  in Fig. 5 is the interval  $T_{\text{flash}}$  during which the flash is happening in Fig. 4—actual values for this simulation are  $\alpha_1 = 45^\circ$ ,  $\alpha_2 = 71.2^\circ$ , and  $T_{\text{flash}} = 437.1 \text{ ms}$ . Note that the base of the straight blade is perpendicular to the propagation direction at  $\alpha_1$ , whereas the tip is orthogonal at  $\alpha_2$ . Also, the part of the flash corresponding to the tip is superposed with the quasi-sinusoidal halo, as shown in Fig. 4.



**Fig. 5.** Approaching straight blade at the instants when its base and tip are perpendicular to the transmitted signal.  $L_b$  is the length of the straight blade.

Fig. 6 represents a zoomed-in view for one flash of the spectrogram result when the aspect angle is  $\theta = 90^\circ$ . Contrary to the case of Fig. 4, the flashes are no longer straight lines as emphasized by the reference straight white line in Fig. 6. Also, the value of the maximum Doppler observed in Fig. 6 has decreased, because the aspect angle has changed ( $\theta = 90^\circ$ ). As a conclusion, it is beneficial to have an aspect angle near to zero ( $\theta \approx 0^\circ$ ). This is because a maximum Doppler excursion and the nonspurious curvature of the flashes are expected in that situation.



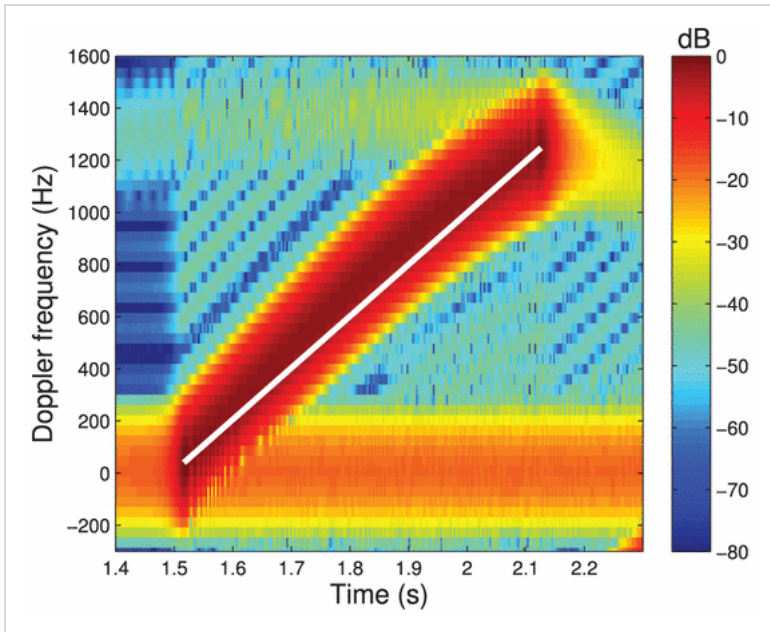


**Fig. 6.** Zoomed-in view for a flash of the spectrogram for straight blades and  $\theta = 90^\circ$ . A white straight line emphasizes that the flash has curvature. Spectrogram parameters: Hamming window of 128 samples and the FFT of 512 points.

### C. Straight Blades for Different Transmitted Frequencies

Straight blades for the wind turbine illuminated by a 24-GHz Doppler radar are considered here. The number of simulated scatterers per blade (20 000) is now higher than the one employed in Fig. 4, since the transmitted frequency has been increased—and hence, the wavelength has been decreased ( $\lambda = 12.5$  mm). The aspect angle for this simulation is  $\theta = 0^\circ$ . The maximum Doppler frequency is now  $f_{\text{Dop,max}} = 2v_{\text{max}}/\lambda = 8377$  Hz, which is again adequately acquired ( $f_s = 20$  kHz).

Fig. 7(a) shows a zoomed-in view for one flash in the spectrogram of Fig. 4, whereas Fig. 7(b) shows a zoomed-in view for the corresponding flash of this section ( $f_c = 24$  GHz). In both the cases, the flash is a straight line as it must be since  $\theta = 0^\circ$ . However, the larger Doppler excursion for the flash in Fig. 7(b) confers a higher resolution in the time-Doppler map upon it. This reveals the advantage of using high-frequency Doppler radars to gain finely detailed spectrograms, where it would be easier to detect possible-arising curvatures in the flashes or other signature features. Thus, the benefit of using a high carrier frequency for the radar sensor comes in terms of improved spectrogram resolution.

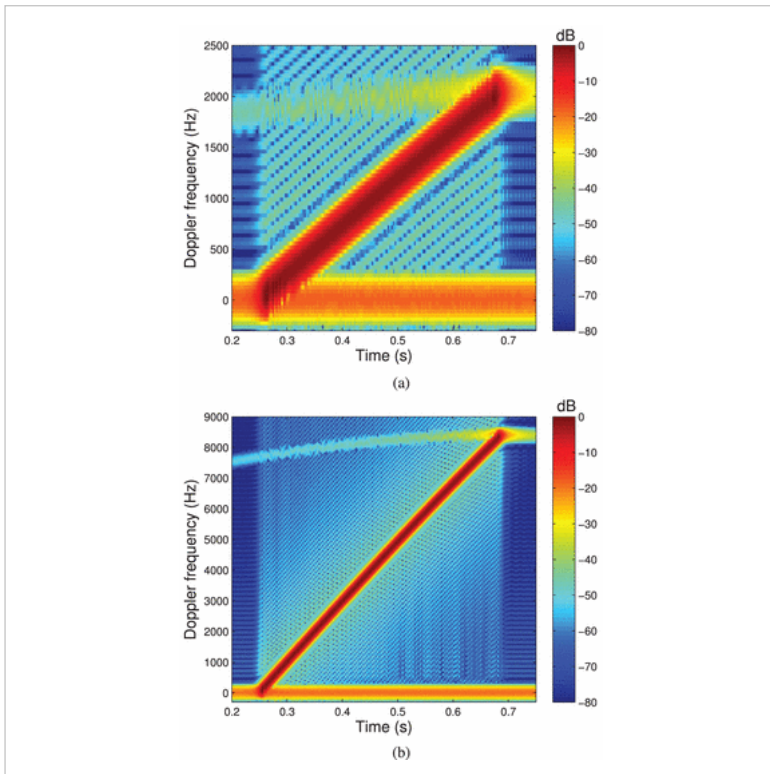
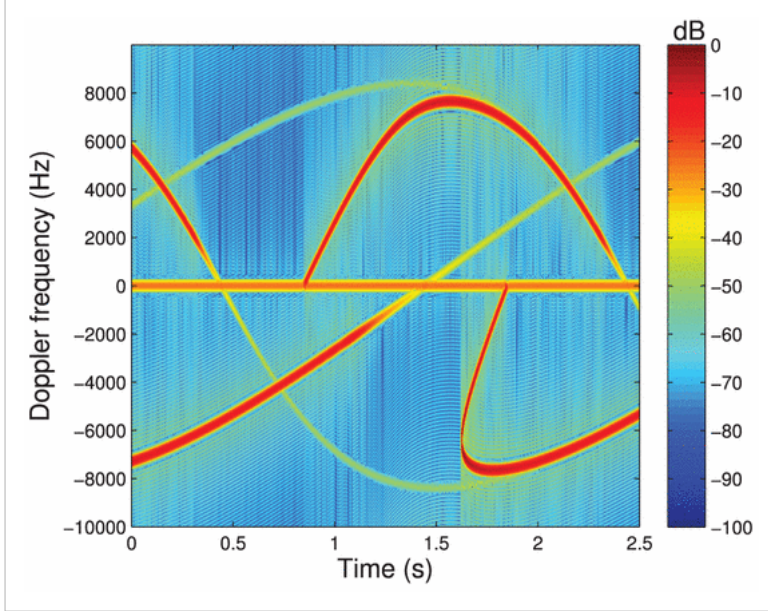


**Fig. 7.** Zoomed-in view for the spectrograms for straight blades and  $\theta = 0^\circ$ . Spectrogram parameters: Hamming window of 128 samples and the FFT of 512 points. (a)  $f_c = 5.8$  GHz. (b)  $f_c = 24$  GHz.

### D. Flashes and Tip Halos for Curved Blades

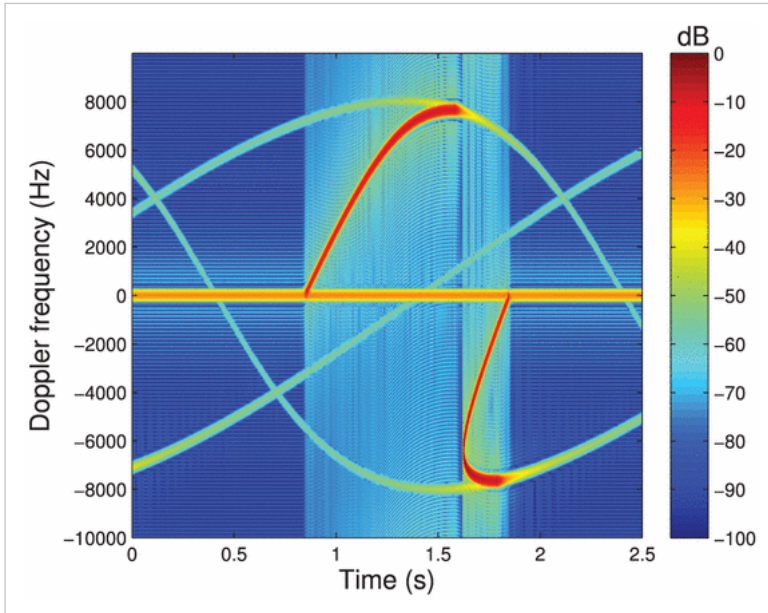
The CW radar frequency is considered here to be 24 GHz—i.e., the wavelength is  $\lambda = 12.5$  mm, which means that the number of the simulated scatterers per blade is 20 000. The orientation angle for the acquisition scenario in Fig. 3 is  $\theta = 0^\circ$ . In addition, the blades are assumed to have a parabolic shape. In particular, in relation to Fig. 2, the vertex coordinates are  $X_v = 10$  m and  $Y_v = 49$  m, and the curvature factor is  $k = 1$ , leading to a distance from the tip to the rotation center of approximately  $R_c = 50$  m (see Table I).

Fig. 8 shows the spectrogram for this situation. As explained in Section II-B, the flash for each blade corresponds to the different contributions of the blade segments when they are perpendicular to the propagation direction of the transmitted signal. Also, the weak quasi-sinusoidal halos for the blade tips are visible. In addition, note that the vertex of the parabola is the tip of the blade ( $k = 1$ ). As detailed in Section II-C, the segment corresponding to the tip becomes orthogonal to the radar emitted signal when the Doppler frequency is zero. This is the reason why the flash describes a curved trajectory in the time-Doppler map that begins in zero Doppler for the blade base and also ends in zero Doppler for the blade tip.



**Fig. 8.** Spectrogram for curved blades ( $X_v = 10$  m,  $Y_v = 49$  m, and  $k = 1$ ) and  $\theta = 0^\circ$ . Spectrogram parameters: Hamming window of 128 samples and the FFT of 512 points.

Fig. 9 shows the spectrogram when  $k = 0.8$ . Note that the quasi-sinusoidal halos are again observed for this value of the curvature parameter. Interestingly, the tip becomes perpendicular to the propagation direction of the transmitted signal when its radial velocity is different from zero. This leads to the characteristic hook shape for the flashes, as it will also be verified through the experiments presented in Section IV.



**Fig. 9.** Spectrogram for curved blades ( $X_v = 10$  m,  $Y_v = 49$  m, and  $k = 0.8$ ) and  $\theta = 0^\circ$ . Spectrogram parameters: Hamming window of 128 samples and the FFT of 512 points.

## E. Simulation of Additional Effects

The point-scatterer model for the baseband signal  $s_b(t)$  in (3) enables the simulation of additional effects in the radar signature of illuminated wind turbines. Here, an  $I/Q$  mismatch is considered. In particular, an amplitude unbalance of 0.5 dB and a phase unbalance of  $5^\circ$  are simulated. In addition, an energetic scatterer ( $\sigma = 100$ ) situated in the middle of each straight blade is also simulated. Note that the addition of this scatterer could consider an echo different from the usual ones corresponding to the smooth surface (e.g., a rivet or a crack). The radar frequency is assumed to be 24 GHz, the number of conventional scatterers per blade is 20 000, and the aspect angle is considered to be  $\theta = 0^\circ$ .



Fig. 10 shows a zoomed-in view for one flash in the spectrogram. For comparison purposes, refer to Fig. 7(b). In addition to the aforementioned flashes and halos, mirrored flashes and additional quasi-sinusoidal Doppler histories due to the energetic scatterers are identifiable. The simulated  $I/Q$  mismatch leads to the echoes mirrored with respect to the zero-Doppler line (i.e., image signals).

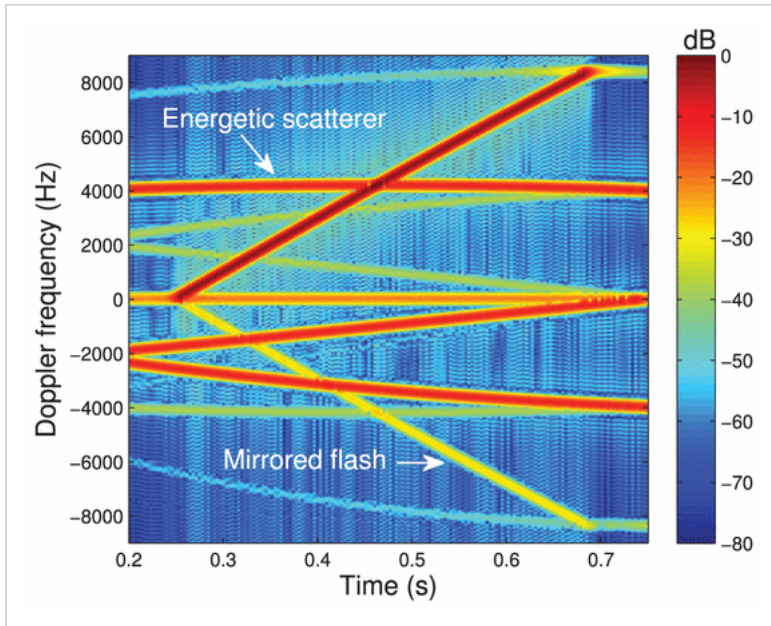


**Fig. 10.** Spectrogram obtained after simulation of some additional effects ( $I/Q$  mismatch and energetic scatterers). Spectrogram parameters: Hamming window of 128 samples and the FFT of 512 points.

## SECTION IV EXPERIMENTAL RESULTS

Two different custom-designed radar systems were used for the acquisition of experimental data. The short-range prototypes operate at the  $C$  and  $K$  bands, respectively. In the next Sections IV-A and IV-B, a brief description of the radar sensors and the acquisition scenario is provided. In addition, the obtained experimental results are evaluated and discussed in the context of the theoretical and simulation frameworks of Sections II and III.

### A. Radar Prototypes

The  $C$ -band radar prototype was designed and implemented by the authors of this paper. It is a portable short-range radar system with reconfiguration capabilities. Indeed, it possesses three modes of operation: the Doppler CW mode, the pure coherent frequency-modulated CW mode, and a hybrid mode, which multiplexes in time the two previous ones. In the context of this paper, only the Doppler mode is exploited. As a Doppler radar, the system uses the two-channel—i.e., stereo—audio jack to acquire the  $I$  and  $Q$  components from a laptop. The audio-card acquisition rate is the conventional audio sampling frequency, i.e.,  $f_s = 44.1$  kHz. The RF and baseband processing units are integrated in two printed circuit boards stacked together. A photograph and a high-level schematic of the radar prototype are provided in Fig. 11(a). As can be seen, the transmitting and receiving antennas are two  $2 \times 2$  patch arrays.

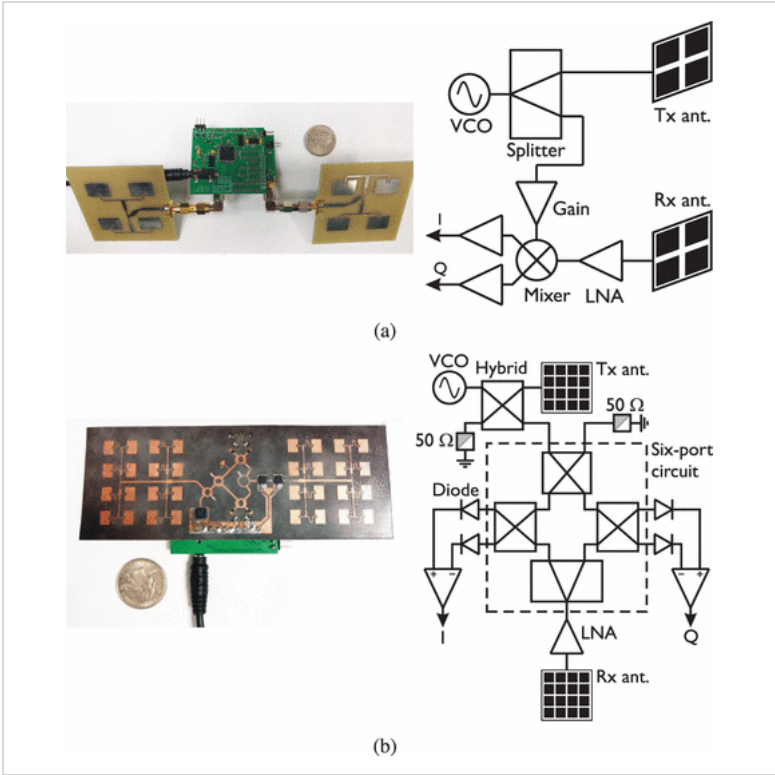


**Fig. 11.** Photographs and high-level schematics of the custom-designed radar prototypes used to illuminate wind turbines (LNA: low-noise amplifier, Rx: reception, Tx: transmission, and VCO: voltage-controlled oscillator). (a) *C*-band radar prototype. (b) *K*-band radar prototype.

On the other hand, the photograph and the block-diagram scheme of the custom-designed *K*-band radar sensor—also implemented by the authors of this paper—are shown in Fig. 11(b). It also has the aforementioned operation modes. To implement the downconversion, a six-port circuit and four detection diodes are employed. Operational amplifiers are used to combine the detected signals and to proceed with the reconstruction of the *I* and *Q* channels. The antennas of this prototype are shaped by  $4 \times 4$  patch arrays.

The main operational parameters of the two Doppler radar systems are listed in Table II.

	C-band radar	K-band radar
Center frequency ( $f_c$ )	5.8 GHz	24 GHz
Wavelength ( $\lambda$ )	51.7 mm	12.5 mm
Transmitted average power	8 dBm	8 dBm
Antenna directivity	11.8 dBi	19.8 dBi
Sampling frequency ( $f_s$ )	44.1 kHz	44.1 kHz

**Table II** Parameters of the Custom-Designed Doppler Radar Prototypes

**B. Acquisition Scenario**

The two radar prototypes in Section IV-A were employed in the American Wind Power Center, Lubbock, TX, USA. There, many wind turbines with various sizes, number of blades, horizontal and vertical rotation axes, and so forth are available. However, considering that the interest of this paper rests in the radar signature of large industrial wind turbines, the experimental results presented here are those corresponding to a 660-kW Vestas V47 wind turbine—which is the largest one in the center and the only modern one of industrial-type—and a 1.9-kW Skystream 3.7 wind turbine—which has three appealing curved blades. A photograph of the in-field wind-turbine acquisition scenario is provided in Fig. 12. The parameters of the illuminated wind turbines are detailed in Table III.



**Fig. 12.** Photograph of the illuminated wind-turbine acquisition scenario in the American Wind Power Center, Lubbock, TX, USA.

	Vestas V47	Skystream 3.7
Rotor diameter	47 m	3.7 m
Blade length ( $L_b$ )	23.5 m	1.8 m
Tower height ( $L_m$ )	50 m	12.2 m
Power	660 kW	1.9 kW

**Table III** Parameters of Illuminated Wind Turbines

**C. Experimental Results for the 660-kW Vestas V47 Wind Turbine**

First, the radar prototypes were situated on the ground under the rotation plane of the Vestas wind turbine—aspect angle  $\theta \simeq 0^\circ$  and  $R_g \simeq 0$  m. Fig. 13 shows the spectrogram for the *C*-band radar. As can be seen, tilted flashes and halos are observable. The positive-Doppler flashes correspond to the approaching blades, whereas the negative-Doppler ones are associated with the receding blades. The rotation period can be estimated from the time appearance of the flashes, leading to  $T \simeq 2.1$  s and an angular speed of  $\Omega \simeq 28.6$  rpm. The maximum Doppler frequency observed in Fig. 13 is  $\sim 2.75$  kHz, which is in close agreement with the theoretical value of  $f_{\text{Dop,max}} = 2\Omega L_b/\lambda = 2718.7$  Hz.

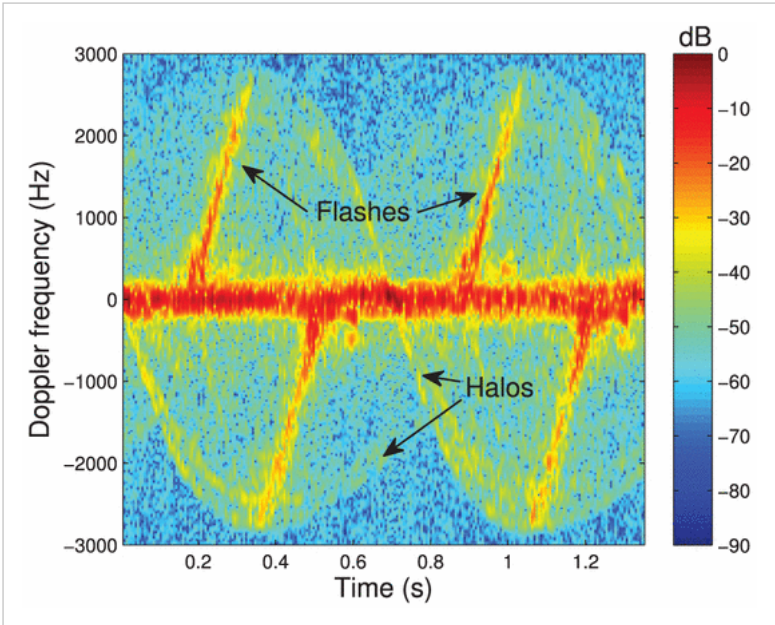


**Fig. 13.** Spectrogram for the Vestas V47 wind turbine illuminated by the  $C$ -band radar prototype ( $\theta \simeq 0^\circ$ ). Spectrogram parameters: Hamming window of 512 samples and the FFT of 4096 points.

A zoomed-in view for one flash in Fig. 13 is shown in Fig. 14. As can be seen, the flash situates quite properly on a linear trajectory in the time-Doppler map. The origin of the additional returns observed in Fig. 14 is attributed to the fact that the blade is a complex 3-D volume.

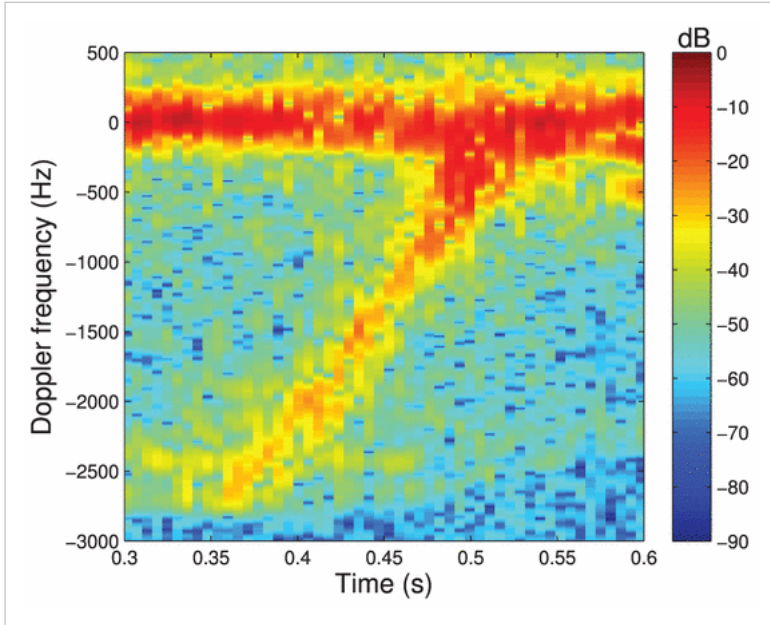


**Fig. 14.** Zoomed-in view for one flash of the spectrogram in Fig. 13.

Fig. 15 details a zoomed-in view for one flash of the experimental spectrogram when the aspect angle has changed to  $\theta \simeq 90^\circ$  and the ground range is about  $R_g \simeq 70$  m. The maximum Doppler frequency for the flash is reduced in comparison with that in Fig. 14. In addition, the determination of a straight trajectory in the time-Doppler map for the flash in Fig. 15 is not as obvious as for the one in Fig. 14, which agrees with the simulations provided in Section III-B. In addition to the geometry change, it is also true that the cross-sectional view of the blades is different for  $\theta \simeq 0^\circ$  and  $\theta \simeq 90^\circ$ . In any case, the experimental results suggest that it is beneficial to have an aspect angle near to zero ( $\theta \simeq 0^\circ$ ), as anticipated in Section III-B.

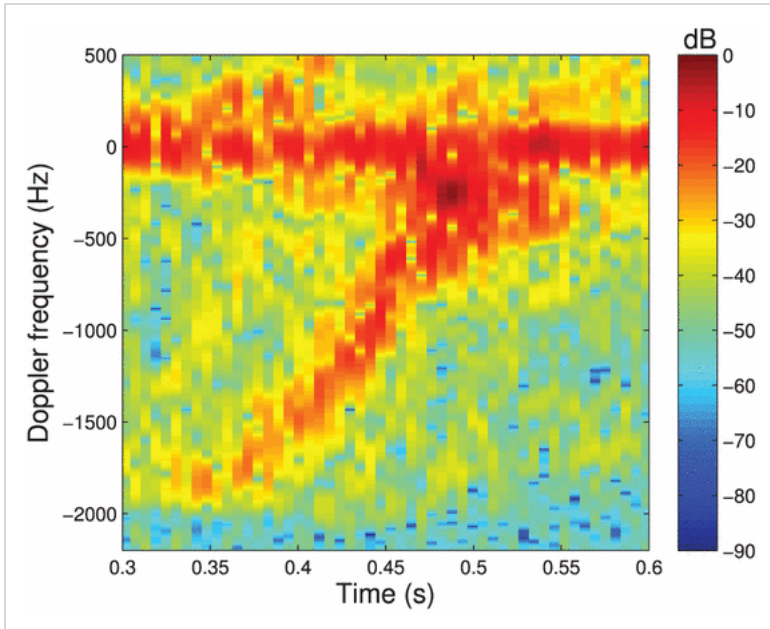


**Fig. 15.** Zoomed-in view for one flash of the spectrogram obtained for the Vestas V47 wind turbine illuminated by the  $C$ -band radar prototype ( $\theta \simeq 90^\circ$ ). Spectrogram parameters: Hamming window of 512 samples and the FFT of 4096 points.

Figs. 16–18 are, respectively, analogous to the previous ones (Figs. 13–15) for the  $K$ -band radar prototype. Interesting differences can be emphasized. First, since the antenna directivity is larger for this 24-GHz radar system (see Table II), the blades are not completely contained within the radar beam. Indeed, these measurements correspond to the manual pointing of the radar at the receding blades, which give rise to negative-Doppler flashes—the positive-Doppler flashes associated with the approaching blades are much less energetic. Second, in terms of the curvature for the flashes, it is again beneficial to have an aspect angle near to zero ( $\theta \simeq 0^\circ$ ) as previously deduced. Third, the use of a higher operation frequency enables to have finely detailed spectrograms with a higher resolution, which is congruent with the simulated results in Section III-C. As a consequence of the latter and in close agreement with Section III-E, additional quasi-sinusoidal histories around the flashes—perhaps due to scattering discontinuities—can be observed in Fig. 17. Besides, the mirrored echoes are attributed to  $I/Q$  mismatches of the  $K$ -band radar sensor, as also shown in Section III-E. Note that the  $C$ -band radar prototype employs a commercial quadrature mixer, which leads to negligible  $I/Q$  mismatches for it.



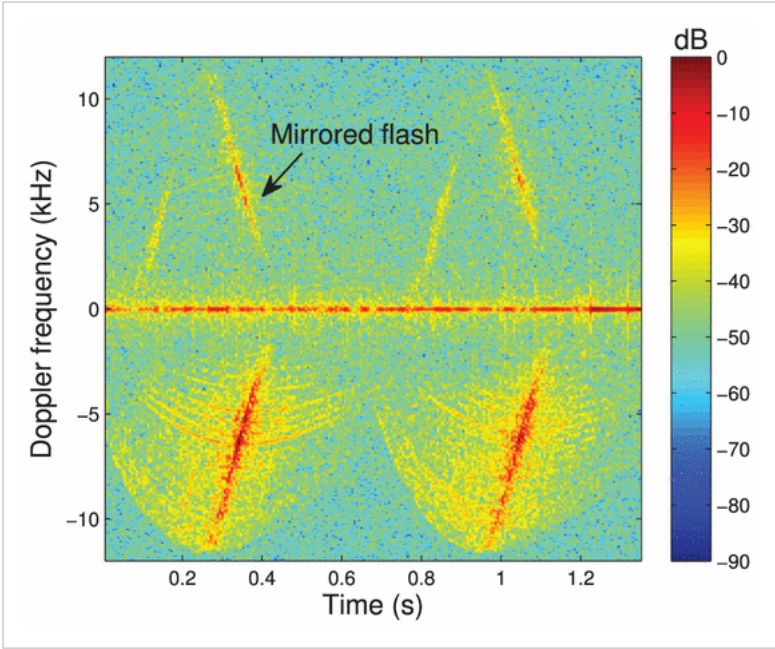


**Fig. 16.** Spectrogram for the Vestas V47 wind turbine illuminated by the  $K$ -band radar prototype ( $\theta \simeq 0^\circ$ ). Spectrogram parameters: Hamming window of 512 samples and the FFT of 4096 points.

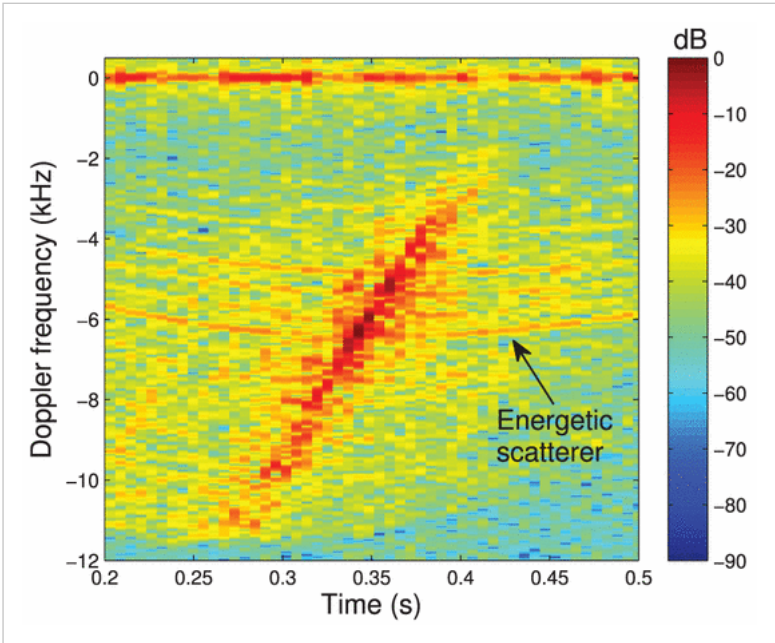


**Fig. 17.** Zoomed-in view for one flash of the spectrogram in Fig. 16.



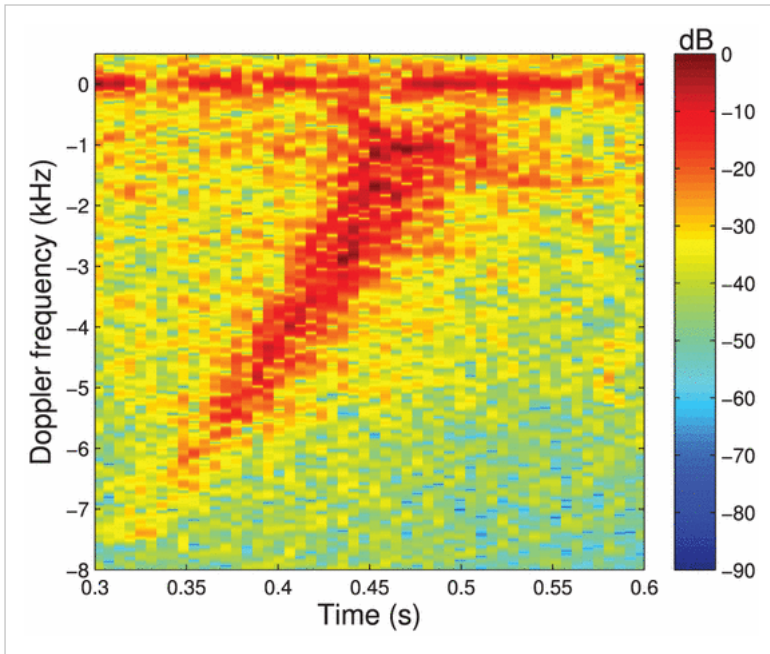
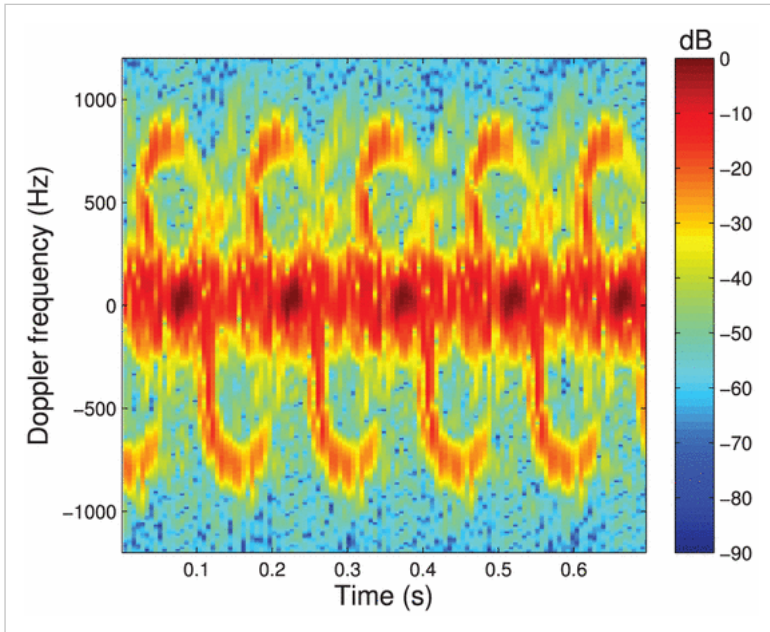


**Fig. 18.** Zoomed-in view for one flash of the spectrogram obtained for the Vestas V47 wind turbine illuminated by the  $K$ -band radar prototype ( $\theta \simeq 90^\circ$ ). Spectrogram parameters: Hamming window of 512 samples and the FFT of 4096 points.

#### D. Experimental Results for the 1.9-kW Skystream 3.7 Wind Turbine

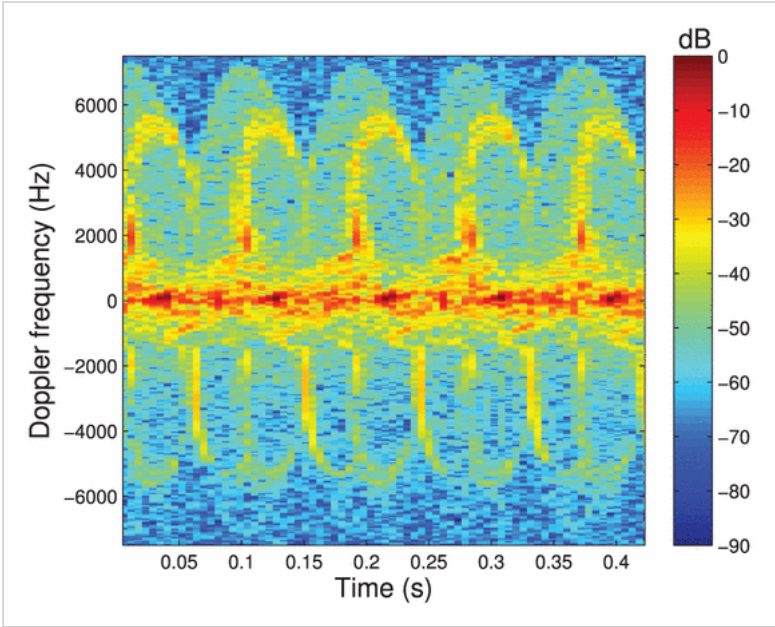
For the data acquisition corresponding to the Skystream 3.7 wind turbine in Fig. 12, the radars were situated on the ground, next to the mast, and below the rotor— $R_g = 0$  m and  $H_r \simeq 2$  m—with an aspect angle of  $\theta = 0^\circ$ .

Fig. 19 shows the spectrogram obtained for the wind turbine when illuminated by the  $C$ -band radar prototype. The radar antennas have wide beams and, thus, the echoes corresponding to the tower and the blades are observable. The hook shape of the flashes permits to validate the parabolic model in Section II-C and the simulations in Section III-D. In fact, one may say that the curvature factor  $k$  for the experiment in Fig. 19 is less than the unity, because the hook does not completely close around zero Doppler—see Sections II-C and III-D. Hence, this  $k$  factor could be used as a measure of the curvature of the blades.



**Fig. 19.** Spectrogram for the Skystream 3.7 wind turbine illuminated by the  $C$ -band radar prototype ( $\theta \simeq 0^\circ$ ). Spectrogram parameters: Hamming window of 512 samples and the FFT of 4096 points.

The experimental results extracted with the  $K$ -band radar sensor are shown in Fig. 20. As can be seen, the hook flashes are again identifiable—especially those associated with the approaching blades. When compared with Fig. 19, the flashes in Fig. 20 have a better resolution in the time-Doppler map—despite their lower energy level, which confirms the convenience of using a high-frequency Doppler radar system to gain finely detailed spectrograms—see Section III-C. As a secondary remark, note that the hooks do not reach the maximum Doppler frequency in the experiments, which is calculated to be  $f_{\text{Dop,max}} = 7045$  Hz for Fig. 20. This has also been observed in the simulations of Section III-D. However, the positive-Doppler quasi-sinusoidal returns in Fig. 20 actually reaches the maximum Doppler frequency. Conversely, the negative-Doppler echoes are not so easily visible, probably due to the manual pointing of the radar prototype and the fact that the radar view of the blades is not the same for receding and approaching blades.



**Fig. 20.** Spectrogram for the Skystream 3.7 wind turbine illuminated by the  $K$ -band radar prototype ( $\theta \simeq 0^\circ$ ). Spectrogram parameters: Hamming window of 512 samples and the FFT of 4096 points.

SECTION V  
CONCLUSION

This paper provided the mathematical framework, simulations, and measurements corresponding to short-range Doppler radar signatures of industrial-type wind turbines, which may be exploited for monitoring purposes. Simple derivations have permitted to justify the spectrogram features (e.g., flashes and tip halos) both for straight and curved blades. It comes to light that it is beneficial to use high-frequency radar systems to improve spectrogram resolution and to capture the data for an aspect angle near zero ( $\theta \simeq 0^\circ$ ), so that the maximum-possible Doppler frequency is obtained and no spurious curvature is observed. Two custom-designed radar prototypes operating at the  $C$  and  $K$  bands have been used to illuminate two straight-and curved-bladed wind turbines in the American Wind Power Center, Lubbock, Texas, USA. The experimental results have confirmed the validity of the expounded theoretical analysis and the performed simulations.

Acknowledgment

The authors would like to thank the American Wind Power Center, Lubbock, TX, USA, for permission to collect and publish data measured from their wind turbines.

FOOTNOTES

The work of J.-M. Muñoz-Ferreras and R. Gómez-García was supported in part by the University of Alcalá under Project CCG-2015/EXP-017 and by the Spanish Ministry of Economy and Competitiveness under Project TEC2014-54289-R. The work of Z. Peng and C. Li was supported by the National Science Foundation under Program ECCS-1254838.

The Associate Editor coordinating the review process was Dr. Mark Yeary.

REFERENCES

1. S. Sawyer and K. Rave  
"Global wind 2014 report"  
*Mar., 2015, Brussels, Belgium*  
[Show Context](#)

2. A. Helmedag, T. Isermann and A. Monti  
"Fault ride through certification of wind turbines based on a hardware in the loop setup"  
*IEEE Trans. Instrum. Meas., vol. 63, no. 10, pp. 2312-2321, Oct., 2014*  
[Show Context](#)

3. Y. Xu, N. Maki and M. Izumi  
"Study of key parameters and cryogenic vessel structure of 10-MW salient-pole wind turbine HTS generators"

*IEEE Trans. Appl. Supercond.*, vol. 25, no. 2, pp. 1-6, Apr., 2015

[Show Context](#)

#### 4. The World' s 10 Biggest Wind Turbines, Featured News

*Kable Intelligence Limited*, Jan., 2014, [online] Available:

<http://www.powertechnology.com>

[Show Context](#)

#### 5. F. Spinato, P. J. Tavner, G. J. W. van Bussel and E. Koutoulakos

"Reliability of wind turbine subassemblies"

*IET Renew. Power Generat.*, vol. 3, no. 4, pp. 387-401, Dec., 2009

[Show Context](#)

#### 6. M. Moradi and S. Sivoththaman

"MEMS multisensor intelligent damage detection for wind turbines"

*IEEE Sensors J.*, vol. 15, no. 3, pp. 1437-1444, Mar., 2015

[Show Context](#)

#### 7. K.-Y. Oh, J.-Y. Park, J.-S. Lee, B. I. Epureanu and J.-K. Lee

"A novel method and its field tests for monitoring and diagnosing blade health for wind turbines"

*IEEE Trans. Instrum. Meas.*, vol. 64, no. 6, pp. 1726-1733, Jun., 2015

[Show Context](#)

#### 8. D. Agarwal and N. Kishor

"A fuzzy inference-based fault detection scheme using adaptive thresholds for health monitoring of offshore wind-farms"

*IEEE Sensors J.*, vol. 14, no. 11, pp. 3851-3861, Nov., 2014

[Show Context](#)

#### 9. A. Ghoshal, M. J. Sundaresan, M. J. Schulz and P. F. Pai

"Structural health monitoring techniques for wind turbine blades"

*J. Wind Eng. Ind. Aerodyn.*, vol. 85, no. 3, pp. 309-324, Apr., 2000

[Show Context](#)

#### 10. C. C. Ciang, J.-R. Lee and H.-J. Bang

"Structural health monitoring for a wind turbine system: A review of damage detection methods"

*Meas. Sci. Technol.*, vol. 19, no. 12, pp. 1-20, Dec., 2008

[Show Context](#)

#### 11. T. Nikoubin, J.-M. Muñoz-Ferreras, R. Gómez-García, D. Liang and C. Li

"Structural health monitoring of wind turbines using a low-cost portable K-band radar: An ab-initio field investigation"

*Proc. IEEE Topical Conf. Wireless Sensors Sensor Netw. (WiSNet)*, pp. 69-71, Jan. 2015, San Diego, CA, USA

[Show Context](#)

#### 12. J.-M. Muñoz-Ferreras, Z. Peng, Y. Tao, R. Gómez-García, D. Liang and C. Li

"A step forward towards radar sensor networks for structural health monitoring of wind turbines"

*Proc. IEEE Topical Conf. Wireless Sensors Sensor Netw. (WiSNet)*, pp. 1-3, Jan. 2016, Austin, TX, USA

[Show Context](#)

#### 13. C. Atzeni, A. Bicci, D. Dei, M. Fratini and M. Pieraccini

"Remote survey of the leaning tower of Pisa by interferometric sensing"

*IEEE Geosci. Remote Sens. Lett.*, vol. 7, no. 1, pp. 185-189, Jan., 2010

[Show Context](#)

#### 14. S. Guan, J. A. Rice, C. Li and C. Gu

"Automated DC offset calibration strategy for structural health monitoring based on portable CW radar sensor"

*IEEE Trans. Instrum. Meas.*, vol. 63, no. 12, pp. 3111-3118, Dec., 2014

[Show Context](#)

#### 15. T. A. Stabile, A. Perrone, M. R. Gallipoli, R. Ditommaso and F. C. Ponzio

"Dynamic survey of the Musmeci bridge by joint application of ground-based microwave radar interferometry and ambient noise standard spectral ratio techniques"

*IEEE Geosci. Remote Sens. Lett.*, vol. 10, no. 4, pp. 870-874, Jul., 2013

[Show Context](#)

#### 16. N. Verma et al

"Enabling scalable hybrid systems: Architectures for exploiting large-area electronics in applications"

*Proc. IEEE*, vol. 103, no. 4, pp. 690-712, Apr., 2015

[Show Context](#)

17. Q. Wang, M. Hong and Z. Su

"An *in-situ* structural health diagnosis technique and its realization via a modularized system"

*IEEE Trans. Instrum. Meas.*, vol. 64, no. 4, pp. 873-887, Apr., 2015

[Show Context](#)

18. H. Z. Hosseinabadi, B. Nazari, R. Amirfattahi, H. R. Mirdamadi and A. R. Sadri

"Wavelet network approach for structural damage identification using guided ultrasonic waves"

*IEEE Trans. Instrum. Meas.*, vol. 63, no. 7, pp. 1680-1692, Jul., 2014

[Show Context](#)

19. K. Perveen, G. E. Bridges, S. Bhadra and D. J. Thomson

"Corrosion potential sensor for remote monitoring of civil structure based on printed circuit board sensor"

*IEEE Trans. Instrum. Meas.*, vol. 63, no. 10, pp. 2422-2431, Oct., 2014

[Show Context](#)

20. M. Lydon et al

"Brien, "Development of a bridge weigh-in-motion sensor: Performance comparison using fiber optic and electric resistance strain sensor systems"

*IEEE Sensors J.*, vol. 14, no. 12, pp. 4284-4296, Dec., 2014

[Show Context](#)

21. Z. Liu and Y. Kleiner

"State-of-the-art review of technologies for pipe structural health monitoring"

*IEEE Sensors J.*, vol. 12, no. 6, pp. 1987-1992, Jun., 2012

[Show Context](#)

22. R. W. Hyers, J. G. McGowan, K. L. Sullivan, J. F. Manwell and B. C. Syrett

"Condition monitoring and prognosis of utility scale wind turbines"

*Energy Mater.*, vol. 1, no. 3, pp. 187-203, Sep., 2006

[Show Context](#)

23. M. A. Rumsey and J. A. Paquette

"Structural health monitoring of wind turbine blades"

*Proc. SPIE Smart Sensor Phenomena, Technol., Netw., Syst.*, pp. 1-15, Mar. 2008, San Diego, CA, USA

[Show Context](#)

24. A. Ghoshal, W. N. Martin, M. J. Schulz, A. Chattopadhyay, W. H. Prosser and H. S. Kim

"Health monitoring of composite plates using acoustic wave propagation, continuous sensors and wavelet analysis"

*J. Reinforced Plastics Compos.*, vol. 26, no. 1, pp. 95-112, Jan., 2007

[Show Context](#)

25. E. Jasinien et al

"NDT of wind turbine blades using adapted ultrasonic and radiographic techniques"

*Insight*, vol. 51, no. 9, pp. 477-483, Sep., 2009

[Show Context](#)

26. S. E. Burrows, A. Rashed, D. P. Almond and S. Dixon

"Combined laser spot imaging thermography and ultrasonic measurements for crack detection"

*Nondestruct. Test. Eval.*, vol. 22, no. 2-3, pp. 217-227, Feb., 2007

[Show Context](#)

27. L. Cheng and G. Y. Tian

"Transient thermal behavior of eddy-current pulsed thermography for nondestructive evaluation of composites"

*IEEE Trans. Instrum. Meas.*, vol. 62, no. 5, pp. 1215-1222, May, 2013

[Show Context](#)

28. H.-L. Fu, K.-C. Fan, Y.-J. Huang and M.-K. Hu

"Innovative optical scanning technique and device for three-dimensional full-scale measurement of wind-turbine blades"

*Opt. Eng.*, vol. 53, no. 12, pp. 1-6, Jul., 2014

[Show Context](#)

29. G. Wild and S. Hinckley

"Acousto-ultrasonic optical fiber sensors: Overview and state-of-the-art"

*IEEE Sensors J.*, vol. 8, no. 7, pp. 1184-1193, Jul., 2008

[Show Context](#)

30. J. M. López-Higuera, L. Rodríguez-Cobo, A. Quintela-Incera and A. Cobo

"Fiber optic sensors in structural health monitoring"

*J. Lightw. Technol.*, vol. 29, no. 4, pp. 587-608, Feb., 2011

[Show Context](#)

31. L. Glavind, I. S. Olesen, B. F. Skipper and M. Kristensen

"Fiber-optical grating sensors for wind turbine blades: A review"

*Opt. Eng.*, vol. 52, no. 3, p. 030901, Mar., 2013

[Show Context](#)

32. A. Naqvi, S.-T. Yang and H. Ling

"Investigation of Doppler features from wind turbine scattering"

*IEEE Antennas Wireless Propag. Lett.*, vol. 9, pp. 485-488, 2010

[Show Context](#)

33. N. Whiteloni, S.-T. Yang and H. Ling

"Application of near-field to far-field transformation to Doppler features from wind turbine scattering"

*IEEE Trans. Antennas Propag.*, vol. 60, no. 3, pp. 1660-1665, Mar., 2012

[Show Context](#)

34. Y. Zhang, A. Huston, R. D. Palmer, R. Albertson, F. Kong and S. Wang

"Using scaled models for wind turbine EM scattering characterization: Techniques and experiments"

*IEEE Trans. Instrum. Meas.*, vol. 60, no. 4, pp. 1298-1306, Apr., 2011

[Show Context](#)

35. A. Naqvi and H. Ling

"Time-frequency and ISAR characteristics of wind turbines with higher order motions"

*Prog. Electromagn. Res.*, vol. 143, pp. 331-347, 2013

[Show Context](#)

36. C. J. Li, R. Bhalla and H. Ling

"Investigation of the dynamic radar signatures of a vertical-axis wind turbine"

*IEEE Antennas Wireless Propag. Lett.*, vol. 14, pp. 763-766, 2015

[Show Context](#)

37. B. M. Kent et al

"Dynamic radar cross section and radar Doppler measurements of commercial general electric windmill power turbines, part 1—Predicted and measured radar signatures"

*IEEE Antennas Propag. Mag.*, vol. 50, no. 2, pp. 211-219, Apr., 2008

[Show Context](#)

38. A. Buterbaugh et al

"Dynamic radar cross section and radar Doppler measurements of commercial general electric windmill power turbines, part 2—Predicted and measured Doppler signatures"

*Proc. Antenna Meas. Techn. Assoc. Symp. (AMTA), St.*, pp. 1-6, Nov. 2007, Louis, MO, USA

[Show Context](#)

39. K. V. Mishra and V. Chandrasekar

"Signal analysis and modeling of wind turbine clutter in weather radars"

*Proc. IEEE Int. Geosci. Remote Sens. Symp. (IGARSS)*, pp. 3561-3564, Jul. 2010, Honolulu, HI, USA

[Show Context](#)

40. I. Angulo et al

"Impact analysis of wind farms on telecommunication services"

*Renew. Sustain. Energy Rev.*, vol. 32, no. 4, pp. 84-99, Apr., 2014

[Show Context](#)

41. O. A. Krasnov and A. G. Yarovsky

"Radar micro-Doppler of wind turbines: Simulation and analysis using rotating linear wire structures"

*Int. J. Microw. Wireless Technol.*, vol. 7, no. 3-4, pp. 459-467, Jun., 2015

[Show Context](#)

42. V. C. Chen

The Micro-Doppler Effect in Radar

2011, Artech House, Norwood, MA, USA

[Show Context](#)



43. F. Nai, R. D. Palmer and S. M. Torres

"Range-Doppler domain signal processing to mitigate wind turbine clutter"

*Proc. IEEE Radar Conf.*, pp. 841-845, May 2011, Kansas City, MO, USA

[Show Context](#)

44. B. Gallardo-Hernando, J. M. Muñoz-Ferreras, F. Pérez-Martínez and F. Aguado-Encabo

"Wind turbine clutter observations and theoretical validation for meteorological radar applications"

*IET Radar Sonar Navigat.*, vol. 5, no. 2, pp. 111-117, Feb., 2011

[Show Context](#)

45. C. Li, V. M. Lubecke, O. Boric-Lubecke and J. Lin

"A review on recent advances in doppler radar sensors for noncontact healthcare monitoring"

*IEEE Trans. Microw. Theory Techn.*, vol. 61, no. 5, pp. 2046-2060, May, 2013

[Show Context](#)

## AUTHORS



### José-María Muñoz-Ferreras

José-María Muñoz-Ferreras (M' 15) received the Telecommunication Engineering and Ph.D. degrees in electrical and electronic engineering from the Polytechnic University of Madrid, Madrid, Spain, in 2004 and 2008, respectively.

He is currently with the Department of Signal Theory and Communications, University of Alcalá, Alcalá de Henares, Spain. His current research interests include radar signal processing, advanced radar systems and concepts, and microwave/RF circuits and systems, specifically focusing on high-resolution inverse synthetic aperture radar images, and the design and validation of radar systems for short-range applications.

Dr. Muñoz-Ferreras is a Reviewer for several IEEE and IET publications. He serves as a member of the Technical Review Board of the IEEE International Geoscience and Remote Sensing Symposium, the IEEE Radar Conference, and the European Radar Conference.

More by this Author: [IEEE Xplore](#)

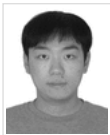


### Zhengyu Peng

Zhengyu Peng (S' 15) received the B.S. and M.Sc. degrees in electrical engineering from Zhejiang University, Hangzhou, China, in 2011 and 2014, respectively. He is currently pursuing the Ph.D. degree in electrical engineering with Texas Tech University, Lubbock, TX, USA.

His current research interests include antennas, microwave circuits, and biomedical applications of microwave/RF circuits and systems.

More by this Author: [IEEE Xplore](#)



### Yao Tang

Yao Tang (S' 15) received the B.S. degree from the University of Electronic Science and Technology of China, Chengdu, China, in 2011. He is currently pursuing the Ph.D. degree in electrical engineering with Texas Tech University (TTU), Lubbock, TX, USA.

He is also with the Department of Electrical and Computer Engineering, TTU. His current research interests include microwave/RF wireless sensors and millimeter-wave radar-system design.

More by this Author: [IEEE Xplore](#)



### Roberto Gómez-García

Roberto Gómez-García (S' 02-M' 06-SM' 11) was born in Madrid, Spain, in 1977. He received the Telecommunication Engineering and Ph.D. degrees in electrical and electronic engineering from the Polytechnic University of Madrid, Madrid, in 2001 and 2006, respectively.

He has been an Associate Professor with the Department of Signal Theory and Communications, University of Alcalá, Alcalá de Henares, Spain, since 2006. He has also been, for several research stays, with the C2S2 Department, XLIM Research Institute, University of Limoges, Limoges, France, the Telecommunications Institute, University of Aveiro, Aveiro, Portugal, the U.S. Naval Research Laboratory, Microwave Technology Branch, Washington, DC, USA, and Purdue University, West Lafayette, IN, USA. His current research interests include the design of fixed/tunable high-frequency filters and multiplexers in planar, hybrid and monolithic microwave integrated circuit technologies, multifunction circuits and systems, and software-defined radio and radar architectures for telecommunications, remote sensing, and biomedical applications.

Dr. Gómez-García is a recipient of the 2016 IEEE MTT-S Young Engineer Award. He serves as a member of the Technical Review Board of several IEEE and EuMA conferences. He is also a member of the IEEE Microwave Theory and Techniques (MTT-S) Filters and Passive Components (MTT-8), the IEEE MTT-S Biological Effect and Medical Applications of RF and Microwave (MTT-10), the IEEE MTT-S Wireless Communications (MTT-20), and the IEEE Circuits and Systems Society Analog Signal Processing Technical Committees. He is an Associate Editor of the IEEE TRANSACTIONS ON MICROWAVE THEORY AND TECHNIQUES and the IET *Microwaves, Antennas and Propagation*, and a Senior Editor of the IEEE JOURNAL ON EMERGING AND SELECTED TOPICS IN CIRCUITS AND SYSTEMS. From 2012 to 2015, he was an Associate Editor of the IEEE TRANSACTIONS ON CIRCUITS AND SYSTEMS I: REGULAR PAPERS. He was a Guest Editor of the IEEE JOURNAL ON EMERGING AND SELECTED TOPICS IN CIRCUITS AND SYSTEMS of the Special Issue on Advanced Circuits and Systems for CR/SDR Applications in 2013, the IET *Microwaves, Antennas and Propagation* of the Special Issue on Advanced Tuneable/Reconfigurable and Multi-Function RF/Microwave Filtering Devices in 2013, and the IEEE *Microwave Magazine* of the Special Issue on Recent Trends on RF/Microwave Tunable Filter Design in 2014. He is a Reviewer of several IEEE, IET, EuMA, and Wiley journals.

More by this Author: [IEEE Xplore](#)

### Daan Liang

Daan Liang received the B.S. degree in engineering management from Tianjin University, Tianjin, China, in 1997, and the M.Sc. and Ph.D. degrees engineering from University at Buffalo, Buffalo, NY, USA, in 1999 and 2001, respectively.



He joined Texas Tech University, Lubbock, TX, USA, in 2004, as an Assistant Professor, where he became an Associate Professor in 2010. In 2014, I appointed as the Interim Director of the National Wind Institute, an intellectual hub for interdisciplinary and transdisciplinary education, research commercialization related to wind science, wind energy, wind engineering, and wind hazard mitigation. His current research interests include win damage assessment, disaster mitigation and recovery, and structural health monitoring of civil structures.

More by this Author: [IEEE Xplore](#)



#### Changzhi Li

Changzhi Li (S' 06–M' 09–SM' 13) received the B.S. degree in electrical engineering from Zhejiang University, Hangzhou, China, in 2004, and the Ph.D. degree in electrical engineering from the University of Florida, Gainesville, FL, USA, in 2009.

He was with Alereon Inc., Austin, TX, USA, and Coherent Logix Inc., Austin, from 2007 to 2009, where he was involved in ultrawideband transceivers and software-defined radio. He joined Texas Tech University, Lubbock, TX, USA, as an Assistant Professor, in 2009, where he became an Associate Professor in 2014. His current research interests include biomedical applications of microwave/RF, wireless sensor, and RF/analog circuits.

Dr. Li received the ASEE Frederick Emmons Terman Award in 2014, the IEEE-HKN Outstanding Young Professional Award in 2014, the NSF Faculty Early CAREER Award in 2013, and the IEEE MTT-S Graduate Fellowship Award in 2008. He received a few best paper awards as an Author/Advisor in the IEEE-sponsored conferences. He is an Associate Editor of the IEEE TRANSACTIONS ON CIRCUITS AND SYSTEMS I. He served as an Associate Editor of the IEEE TRANSACTIONS ON CIRCUITS AND SYSTEMS II in 2014 and 2015. He served as the Technical Program Committee Co-Chair of the IEEE Wireless and Microwave Technology Conference in 2012 and 2013.

More by this Author: [IEEE Xplore](#)

## CITED BY

None

## KEYWORDS

### IEEE Keywords

Blades, Doppler radar, Mathematical model, Monitoring, Spectrogram, Wind turbines

### INSPEC: Controlled Indexing

Doppler radar, blades, condition monitoring, mathematical analysis, portable instruments, radar equipment, sensors, structural engineering, wind turbines

### INSPEC: Non-Controlled Indexing

curved-blade wind turbine, high-frequency radar system, improved spectrogram resolution, industrial wind turbine, industrial-type wind turbine, mathematical analysis, noncontact structural health monitoring, nonstraight blade, portable low-cost Doppler radar sensor, short-range Doppler-radar signal signature, size 12 m, size 50 m, time-Doppler map

### Authors Keywords

Doppler radars, flashes, spectrogram, structural health monitoring (SHM), wind turbine, wireless sensors

## CORRECTIONS

None

IEEE Account

- » Change Username/Password
- » Update Address

Purchase Details

- » Payment Options
- » Order History
- » View Purchased Documents

Profile Information

- » Communications Preferences
- » Profession and Education
- » Technical Interests

Need Help?

- » **US & Canada:** +1 800 678 4333
- » **Worldwide:** +1 732 981 0060
- » Contact & Support

About IEEE *Xplore* | Contact Us | Help | Terms of Use | Nondiscrimination Policy | Sitemap | Privacy & Opting Out of Cookies

A not-for-profit organization, IEEE is the world's largest technical professional organization dedicated to advancing technology for the benefit of humanity.  
© Copyright 2017 IEEE - All rights reserved. Use of this web site signifies your agreement to the terms and conditions.